Titanium Substitution to Advance the Prospect of $NaMnO_2$ Cathodes for Practical Application in Sodium-Ion Batteries

Siyu An[1], Rajib Sahu[1,2], Ruizhuo Zhang[1], Fatih Ulusoy[1], Christian Kübel[2,3], Aleksandr Kondrakov[1,4]*, Jürgen Janek,[1,5] and Torsten Brezesinski[1]*

[1]Battery and Electrochemistry Laboratory (BELLA), Institute of Nanotechnology, Karlsruhe Institute of Technology (KIT), Kaiserstr. 12, 76131 Karlsruhe, Germany

[2]Karlsruhe Nano Micro Facility (KNMFi), Institute of Nanotechnology (INT), Karlsruhe Institute of Technology (KIT), Kaiserstr. 12, 76131 Karlsruhe, Germany

[3]Institute of Materials Science, Technical University Darmstadt (TUDa), Peter-Grünberg-Str. 2, 64287 Darmstadt, Germany

[4]BASF SE, Carl-Bosch-Str. 38, 67056 Ludwigshafen, Germany

[5]Institute of Physical Chemistry & Center for Materials Research (ZfM/LaMa), Justus-Liebig-University Giessen, Heinrich-Buff-Ring 17, 35392 Giessen, Germany

*Corresponding authors: aleksandr.kondrakov@basf.com, torsten.brezesinski@kit.edu

Abstract

O3-type layered oxides stand out among various Na-ion battery cathodes due to their unparalleled theoretical specific capacities. As a representative of low-cost, Mn-based cathode materials, *α*-$NaMnO_2$ (NMO) has attracted great attention. However, its practical application is hindered by poor reversibility. Compared to other O3 or O'3-type layered oxides, such as $NaNiO_2$, NMO undergoes multiple phase transitions, with the final O1 phase negatively affecting cycling performance. In this study, precipitated Mn_3O_4 was employed, to our knowledge for the first time, as a precursor in the synthesis of NMO, and the cathode material was systematically optimized through incremental improvement via titanium substitution. $NaMn_{0.9}Ti_{0.1}O_2$ was found to exhibit enhanced stability, with the capacity retention increasing from 42 to 70 % after 50 cycles at C/10, along with superior rate capability over NMO. This is due in part to titanium's role in facilitating primary particle (grain) growth and suppressing O1 phase formation, thereby preserving structural integrity and mitigating degradation caused by volume variations and irreversible oxygen redox during battery operation. This work not only provides valuable insights into the development of next-generation NMO cathodes but also advances their potential for practical applications.

Keywords: SIB cathode, titanium substitution, single-crystalline morphology, chemo-mechanical degradation, outgassing

Introduction

Electrochemical energy-storage devices (EESDs) are now widely employed across various applications, ranging from small-scale electronic products to large-scale grid energy-storage systems and electric vehicles, and have become indispensable in modern society. Lithium-ion batteries (LIBs) as one of the most widely used type of EESDs have been extensively studied and applied.[1–5] However, the uneven distribution of lithium resources and their increasing demand highlight the urgent need for alternative and more sustainable solutions to address these challenges.[6–8]

Nowadays, attention has been re-directed toward various alkali-metal batteries.[9–12] In this regard, sodium-ion batteries (SIBs) offer major advantages in terms of reversible capacity, kinetics, thermo-chemical stability, and ease of storage and transportation. Given the conceptual and functional similarities between SIBs and LIBs, the development and production of SIBs face fewer technical barriers.[13–16] As a result, SIBs have re-gained attention, particularly in applications where energy density constraints related to volume or weight are less critical.

Among the cathode materials for SIBs, layered sodium transition-metal (TM) oxides ($NaTMO_2$) have emerged as the most promising candidates due to their high theoretical specific capacities. Unlike lithium in layered oxides, occupying only octahedral sites, Na^+ ions can reside on prismatic or octahedral sites coordinated by six oxygen ions, thus forming two primary structure types, namely P2 and O3.[17–21] Mn-based layered oxides are particularly attractive for cost reasons (abundant raw material availability).[8,22,23] Among them, the P2-type $Na_{0.7}MnO_2$ has been widely explored for its excellent rate performance. However, the intrinsic sodium deficiency of the P2 structure poses challenges for practical applications.[24,25] To address this issue, researchers have proposed employing sacrificial salts, such as Na_2CO_3, to compensate for sodium deficiencies.[26,27] However, the large quantities of CO_2 generated by Na_2CO_3 during electrochemical cycling render this approach impractical.[27] Therefore, O3-type layered oxides with relatively higher sodium contents, such as $NaMnO_2$ (NMO), hold greater potential for practical deployment.[2,28]

Stoichiometric NMO exists in two polymorphs, the low-temperature alpha phase and the high-temperature beta phase. The alpha phase undergoes structural distortion, from *R*−3*m* to monoclinic *C*2/*m* symmetry, due to the Jahn-Teller effect of high-spin Mn^{3+}, forming an O'3-type structure. By contrast, the beta phase adopts a zigzag structure.[29–31] Density functional theory (DFT) calculations by Shishkin *et al.* indicate that the formation energies of both phases are nearly identical, making it challenging to obtain a single-phase material.[30]

Regarding cycling performance, Ma *et al.* demonstrated a reversible specific capacity of about 200 mAh/g for *α*-NMO in 2011.[2] Further work by Manzi *et al.* on both the high- and low-temperature phases revealed that *α*-NMO exhibits better reversibility for sodium insertion/extraction.[29] Consequently, the *α*-phase, which is easier to synthesize with high purity, holds more potential for practical applications. Nevertheless, the poor

cyclability of *α*-NMO remains a critical issue. To investigate the underlying reasons, Kubota *et al.* carried out *in situ* and *ex situ* X-ray diffraction (XRD) analyses on *α*-NMO and identified the formation of a mixed O'3-O1 phase with reduced interlayer spacing at high potentials.[31] Based on the phase evolution, further studies on the voltage window revealed that a narrower range of 2–3.476 V, compared to 2–3.8 V, increases stability by preventing formation of the O'3-O1 phase. Additionally, cycling in a wider range of 2–3.8 V was found to lead to (irreversible) changes in crystallinity, which can further compromise performance.[31] Therefore, suppressing or avoiding O1 phase formation appears critical to enhancing stability.

One common strategy to suppress phase transitions is the substitution of TM ions in $NaTMO_2$.[32–34] The same holds for LIB cathode materials. For NMO, TM substitution not only helps suppress phase transitions but also to stabilize specific polymorphs. Shishkin *et al.* investigated the substitution of manganese in NMO with 12 different elements and found that titanium and copper are able to effectively stabilize *α*-NMO and *β*-NMO, respectively.[30] However, systematic studies on Ti^{4+}-substituted, Mn-rich O'3-type NMO are lacking.

In the present work, we substituted manganese in NMO with varying fractions of Ti^{4+} and systematically investigated the structure, morphology, and electrochemical performance of the respective cathode materials. Ultimately, we identified $NaMn_{0.9}Ti_{0.1}O_2$ (NMTO) as the optimal composition. Results from XRD and differential electrochemical mass spectrometry (DEMS) measurements demonstrate that the introduction of titanium successfully suppresses the formation of the O1 phase at high potentials and partially inhibits irreversible lattice oxygen redox. Furthermore, it facilitates grain growth and coarsening during calcination, eventually resulting in the formation of quasi single-crystal particles with enhanced cycling stability.

Results and Discussion

In contrast to most studies that typically employ Mn_2O_3 as a precursor in the synthesis, Mn_3O_4 precipitated from solution (see scanning electron microscopy [SEM] image and XRD pattern in **Figure S1**, Supporting Information) was used here to improve the electrode's tap density.[2,29–31,35] First, NMO was prepared to validate the feasibility of the experimental conditions for the new precursor. To this end, Mn_3O_4 and Na_2CO_3 (5 mol.% excess) were thoroughly blended, followed by calcination at 800 °C for 12 h under air. Finally, the material was quenched to room temperature, yielding NMO. The XRD pattern collected from the as-synthesized sample is presented in **Figure 1a**. Rietveld analysis confirmed that the material is single phase and crystallizes in a monoclinic (*C*2/*m*) structure with lattice parameters *a* = 5.666(2) Å, *b* = 2.8602(1) Å, *c* = 5.803(2) Å, and *β* = 113.174(5)° (**Table S1**, Supporting Information), in agreement with reports available in the literature.[2,31] An SEM image of NMO is shown in **Figure 1b**, revealing that the primary particles exhibit a rod-like shape and the secondary particles are of spherical morphology.

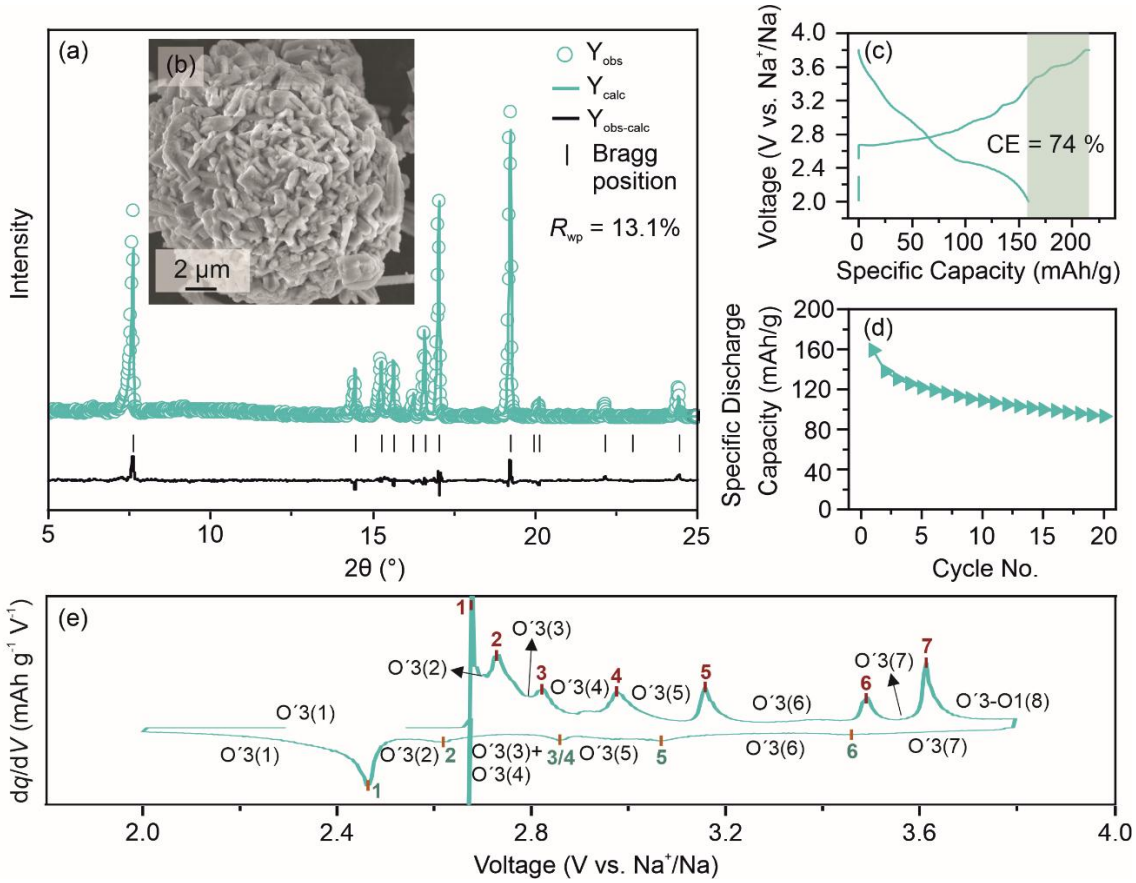

Figure 1. (a) XRD pattern and Rietveld refinement, (b) SEM image, (c) first-cycle voltage profile, (d) cycling performance at C/10, and (e) first-cycle differential capacity curve of $NaMnO_2$ (NMO). Peaks for the oxidation process (1–7) are marked in red and those for the reduction process (1–6) in green in panel (e).

The first-cycle voltage profile of NMO cycled in a SIB half-cell is displayed in **Figure 1c**. The initial specific charge and discharge capacities reached 216 and 160 mAh/g, respectively, corresponding to a Coulomb efficiency of 74 % (2.0–3.8 V vs. Na^+/Na, C/10). Notably, the discharge capacity was slightly lower than previously reported.[31,36] This discrepancy may be attributed to the large primary particle size, negatively affecting sodium transport. However, the electrolyte used may also play a role.[37] Regardless, it should be noted that large primary particles may contribute to a less distinct voltage profile (due to the presence of inherent inhomogeneities).[31]

The cycling stability over 20 cycles (58 % capacity retention) and the first-cycle differential capacity (d*q*/d*V*) curve are shown in **Figures 1d** and **e**, respectively. The d*q*/d*V* data successfully reproduce the seven oxidation peaks and five reduction peaks reported in the literature. Both the O'3(3) and O'3(5) correspond to triclinic phases, while the remaining six phases are monoclinic in nature. Although the third oxidation peak does not have a (distinct) respective reduction peak, Komaba and co-workers observed the presence of some O'3(3) at the O'3(4) position in **Figure 1e**.[31] Overall, the XRD and electrochemical results are consistent with previous reports, confirming the successful synthesis of single-phase NMO using precipitated Mn_3O_4 as a precursor.

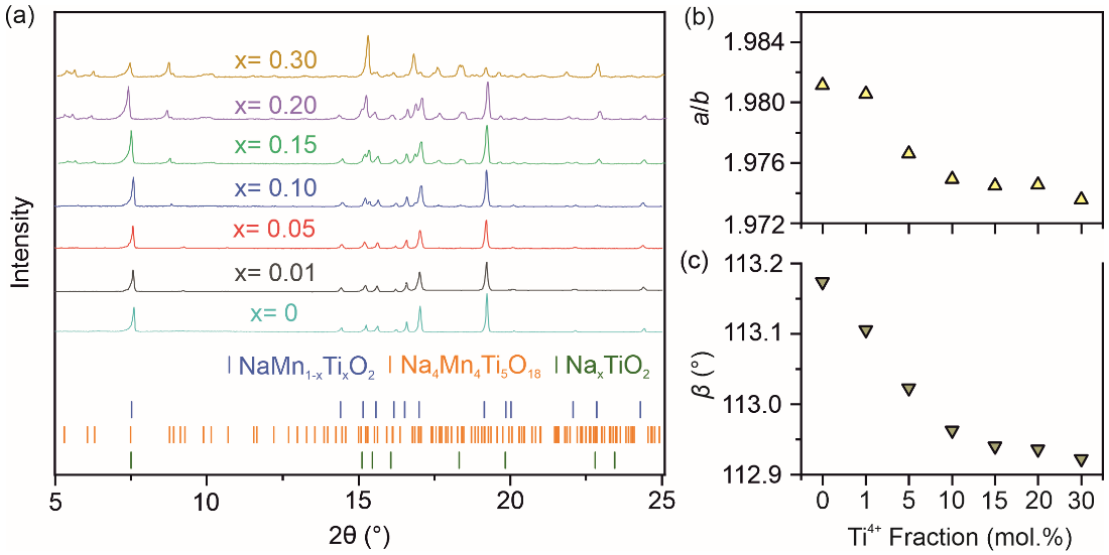

Figure 2. (a) XRD patterns of $NaMnO_2$ (NMO) and $NaMn_{1-x}Ti_xO_2$, with x = 0.01, 0.05, 0.10, 0.15, 0.20, and 0.30. Corresponding (b) *a*/*b* and (c) *β* values from Rietveld analyses.

Ti^{4+}-substituted NMO ($NaMn_{1-x}Ti_xO_2$) was prepared under identical conditions by substituting manganese with titanium. In this study, six different titanium fractions, namely 1, 5, 10, 15, 20, and 30 mol.%, were investigated to explore the effect that substitution has on the structure and cycling performance of NMO. **Figure 2a** presents the XRD patterns for the different samples, and the phase fractions from Rietveld analyses are given in **Table S2** (Supporting Information). As evident, impurity phases, such as $Na_4Mn_4Ti_5O_{18}$ (*Pbam*) and Na_xTiO_2 (*R*−3*m*), start to appear with increasing degree of substitution (starting from about 5 mol.% Ti^{4+}). When the titanium fraction reaches 30 mol.%, the target phase, $NaMn_{1-x}Ti_xO_2$ (*C*2/*m*), only accounts for 10(1) wt.%. Collectively, these results indicate that moderate substitution levels effectively stabilize the *α*-NMO, while excessive Ti^{4+} incorporation promotes the formation of secondary phases.[35]

Table S1 (Supporting Information) summarizes the structural parameters derived from Rietveld refinements, and **Figures 2b** and **c** display the trends in *a*/*b* ratio and *β* with increasing titanium fraction. The *a*/*b* ratio is commonly used to quantify the degree of in-plane distortion in layered materials, where an undistorted hexagonal structure has a value of $\sqrt{3}$.[31,34] As can be seen from **Figure 2b**, the *a*/*b* ratio decreases with increasing degree of substitution and stabilizes around 10 mol.% Ti^{4+}. A similar trend is observed for *β* in **Figure 2c**. These results indicate that the Jahn-Teller distortion caused by high-spin Mn^{3+} is effectively mitigated. A possible reason for this is that the introduction of Ti^{4+} induces the formation of an equivalent amount of Mn^{2+}, a phenomenon we also observed in a previous study on $NaNi_{0.9}Ti_{0.1}O_2$.[34,38] The plateau in the *a*/*b* and *β* data beyond 10 mol.% Ti^{4+} is likely due to the solubility limit being reached.

Results from inductively coupled plasma-optical emission spectroscopy (ICP-OES) measurements conducted on the $NaMn_{1-x}Ti_xO_2$ with x = 0, 0.01, 0.05, and 0.10 are given in **Table S3** (Supporting Information), indicating that all materials had the intended composition with minimal sodium losses.

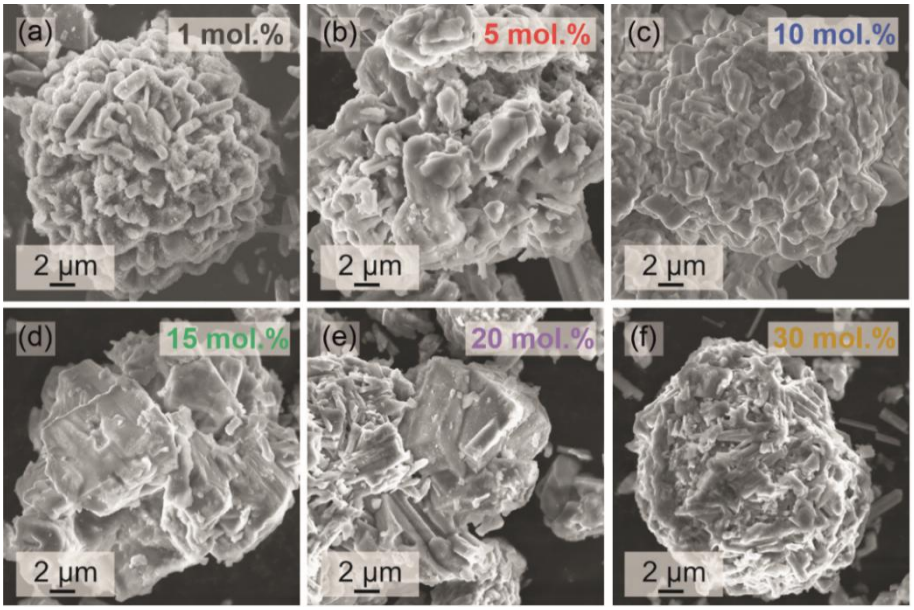

Figure 3. (a–f) SEM images of $NaMn_{1-x}Ti_xO_2$, with x = 0.01, 0.05, 0.10, 0.15, 0.20, and 0.30.

Figures 3a–f show SEM images of the $NaMn_{1-x}Ti_xO_2$ samples. All of them retained, to varying degrees, a secondary particle morphology. However, significant differences were observed in the size and morphology of primary particles (grains). With increasing titanium fraction, the grains grow much larger, evolving from elongated shapes into quasi single-crystal particles. Similar observations have been made for layered LIB cathodes. For example, cobalt doping tends to increase particle size, whereas selenium or tungsten doping can suppress grain growth of lithium transition-metal oxides.[39–41] This can be attributed to the ability of different dopants/substituents to affect surface energy, thereby regulating the grain growth orientation during synthesis.[39] Note that in **Figures 3e** and **f**, the smaller particles present on the surface are likely impurity phases, such as $Na_4Mn_4Ti_5O_{18}$ and/or Na_xTiO_2. These findings clearly demonstrate that Ti^{4+} substitution has a profound effect on both the morphology and size of NMO grains.

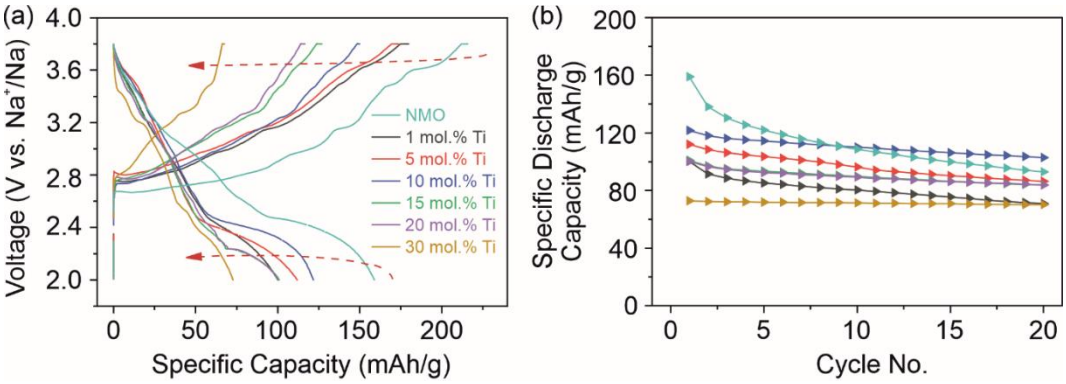

Figure 4. (a) First-cycle voltage profile of SIB half-cells using either $NaMnO_2$ (NMO) or $NaMn_{1-x}Ti_xO_2$, with x = 0.01, 0.05, 0.10, 0.15, 0.20, and 0.30, at C/10 and (b) corresponding cycling performances.

Subsequently, the electrochemical performance of the $NaMn_{1-x}Ti_xO_2$ samples was evaluated to further investigate the influence of Ti^{4+} substitution on NMO. **Figure 4a** presents the respective first-cycle voltage profiles (2.0–3.8 V vs. Na^+/Na, C/10), showing that the specific charge capacity decreases with increasing titanium fraction. Due to the differences in phase purity, further discussion needs to be divided into the following cases. For ≤ 10 mol.% Ti^{4+}, two potential reasons may explain the observed capacity decline. First, the larger primary particles may slow down sodium diffusion. Second, varying degrees of lattice distortion, as indicated by the changes in *a*/*b* ratio, may affect the Na^+ extraction. For example, previous studies have shown that P'2-Na_xMnO_2 (with lattice distortion) delivers higher reversible capacities than P2-Na_xMnO_2.[24] For > 10 mol.% Ti^{4+}, the capacity is strongly determined by the impurity phase $Na_4Mn_4Ti_5O_{18}$, which itself is electrochemically active (with decreasing contribution from $NaMn_{1-x}Ti_xO_2$).

As can be seen from **Figure 4a** and **Figure S2** (Supporting Information), the first-cycle specific discharge capacity exhibits a more intriguing trend. It decreased gradually upon exceeding 10 mol.% Ti^{4+}, due to increasing fraction of impurity phases. For ≤ 10 mol.% Ti^{4+}, it first decreased and then increased with increasing substitution level, reaching a local maximum around 10 mol.%. Interestingly, the sample containing 1 mol.% Ti^{4+} delivered the lowest capacity, which is likely related to the primary particle size. However, the 5 and 10 mol.% Ti^{4+} samples with even larger grains exhibited superior discharge capacities. This is also evident from the dq/dV plots presented in **Figure S3** (Supporting Information). It is worth noting that due to the large polarization in the initial cycle, the curves for the second cycle are presented instead. With increasing titanium fraction, additional peaks emerged, especially so for the sample containing 10 mol.% Ti^{4+}. Guo *et al.* reported that $Na_4Mn_4Ti_5O_{18}$ shows redox peaks at 3.4/3.3 and 2.4/2.3 V vs. Na^+/Na, indicating that it is electrochemically active in the voltage window employed here for testing the $NaMn_{1-x}Ti_xO_2$ cathodes.[42] Nevertheless, comparative analysis revealed that the redox peaks of $Na_4Mn_4Ti_5O_{18}$ do not correspond to any of the features observed in the differential capacity curves. Furthermore, the phase fraction of $Na_4Mn_4Ti_5O_{18}$ (with 10 mol.% Ti^{4+}) only accounted

for 4.1(5) wt.% (**Table S2**, Supporting Information), making it unlikely to significantly contribute to the capacity. This in turn suggests that the newly observed peaks mainly originate from the $NaMn_{0.9}Ti_{0.1}O_2$ cathode material itself.

The *ex situ* Ti K-edge X-ray absorption near-edge structure spectroscopy (XANES) data in **Figure S4** (Supporting Information) provide further insights. For the 10 mol.% Ti^{4+} sample, the energy positions during charging and discharging remained unaltered upon electrochemical cycling, indicating that titanium only serves as a structural stabilizer without exhibiting redox activity. This can imply that the above observations may be due to variations in local manganese environment and/or sodium/vacancy ordering. Indeed, previous studies on NMO revealed the presence of $Mn^{3+/4+}$ ordering and Na^+/vacancy ordering.[28] Therefore, the additional peaks in the d*q*/d*V* plots seem to directly result from the Ti^{4+} incorporation, affecting the manganese valence-state distribution and leading to distinct $Mn^{2+/3+/4+}$ ordering and/or Na^+/vacancy ordering. Of note, as expected, similar peak patterns were observed for samples with higher titanium fractions (**Figure S3**, Supporting Information).

Figure 4b illustrates the cycling stability of the $NaMn_{1-x}Ti_xO_2$ samples. The one having 10 mol.% Ti^{4+} exhibited the best overall performance, maintaining a high specific discharge capacity of q_{dis} > 100 mAh/g and achieving a capacity retention of 85 % after 20 cycles at C/10, compared to only 58 % observed for NMO. **Figure S5** (Supporting Information) presents the corresponding voltage profiles for the 2nd, 10th, and 20th cycles. As can be seen from this data, the 10 mol.% Ti^{4+} sample showed relatively low polarization during cycling, indicating improved sodium transport properties. Those containing 15, 20, and 30 mol.% Ti^{4+} also revealed reduced polarization. However, this is likely due to the high fraction of impurity phases, which is also why they delivered much lower reversible capacities. Based on these results, further investigations focused on the 10 mol.% Ti^{4+} sample, which will be referred to as NMTO in subsequent discussions.

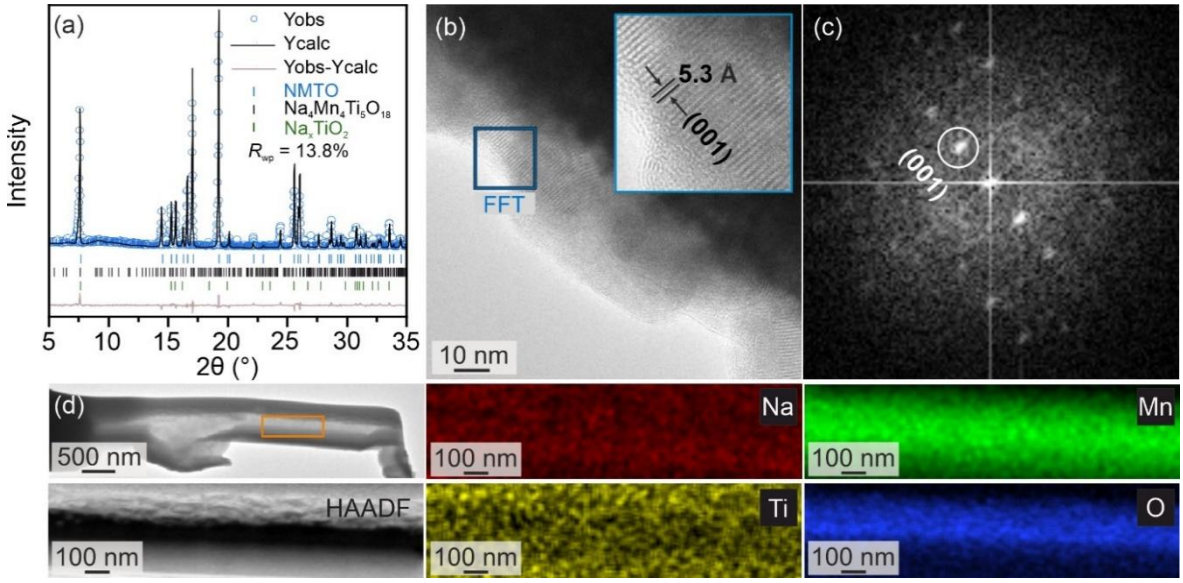

Figure 5. (a) XRD pattern and Rietveld refinement, (b) HRTEM image, and (c) FFT pattern from the region highlighted by the blue box in (b) of $NaMn_{0.9}Ti_{0.1}O_2$ (NMTO). (d) Corresponding STEM-EDS mapping analysis.

XRD and transmission electron microscopy (TEM) measurements were conducted on the NMTO to examine its structural and chemical characteristics in some more detail (**Figures 5a–d**). **Figure 5b** presents a high-resolution TEM (HRTEM) image, clearly revealing its layered nature. Fast Fourier transformation (FFT) analysis identified characteristic lattice planes of spacing 5.3 Å (**Figure 5c**), consistent with the results from Rietveld refinement of XRD data (**Figures 5a**). **Figure 5d** shows scanning TEM (STEM) images of a focused ion beam (FIB)-cut cross-section of an NMTO particle and corresponding energy dispersive X-ray spectroscopy (EDS) maps, with the latter suggesting homogeneous distribution of elements across the sample. However, we note that some non-uniformities in composition were also observed (**Figure S6**, Supporting Information). This result agrees with the presence of Na_xTiO_2 as an impurity phase. Because of the similar elemental composition of $Na_4Mn_4Ti_5O_{18}$ and the NMTO phase, distinguishing their spatial distribution via EDS alone is very challenging.

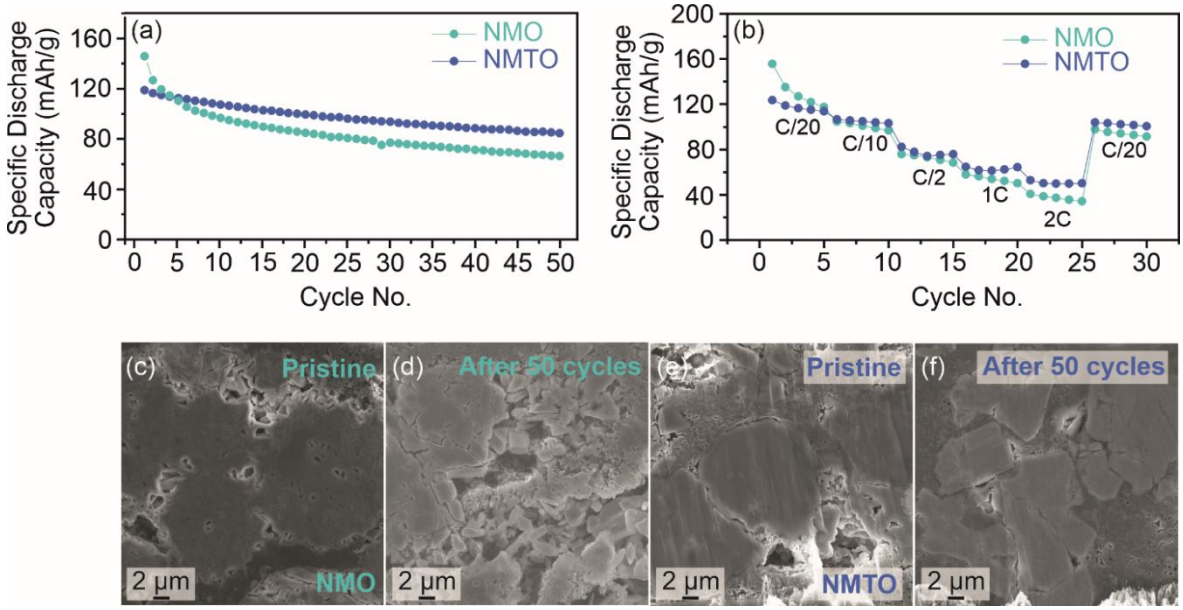

Figure 6. Comparison of (a) cycling performance at C/10 and (b) rate capability of $NaMnO_2$ (NMO) and $NaMn_{0.9}Ti_{0.1}O_2$ (NMTO) in SIB half-cells. Cross-sectional SEM images of (c, e) pristine and (d, f) cycled cathodes.

The cycling performance of the NMO and NMTO cathodes over 50 cycles at C/10 is shown in **Figure 6a**. In the case of NMTO, the capacity retention was about 70 %, compared to 42 % for NMO, indicating that the introduction of Ti^{4+} enhances the stability. **Figure 6b** presents the rate capability of NMTO and NMO. Notably, an initial current rate of C/20 was employed to investigate whether this helps extract more capacity. However, the first-cycle specific discharge capacities were found to be similar to those achieved with the same cathodes at C/10 in **Figure 6a**. This observation

agrees with previous reports on NMO,[2] indicating that the sodium diffusion kinetics is not the primary factor limiting the accessible (reversible) capacity at low current density. It is worth noting that, apart from the initial five cycles at C/20, NMTO consistently delivered higher capacities, with lower polarization (**Figure S7**, Supporting Information) across various current rates as compared to NMO. This can be explained by the interslab distances given in **Table S1** (Supporting Information). However, it should be noted that calculations were only made for samples with ≤ 10 mol.% Ti^{4+} because of their relatively higher phase purity. The results demonstrate that the interslab distance increases with increasing titanium fraction, which in turn facilitates sodium diffusion and enhances rate performance. Note that the latter increase is not due to changes in ionic radius (Ti^{4+}: r = 0.605 Å, Mn^{3+}: r = 0.645 Å, Mn^{2+}: r = 0.83 Å) but reduced Jahn-Teller distortion.

Figures 6c–f show cross-sectional SEM images of NMO and NMTO cathodes before and after long-term cycling. In **Figure 6c**, the primary particles within the secondary particles of NMO can be clearly distinguished, and they appear closely packed. However, after 50 cycles (**Figure 6d**), severe intergranular cracking was evident. This suggests that, during battery operation, reactive surfaces are formed and continuously exposed to the electrolyte, thereby accelerating degradation. By contrast, NMTO with its quasi single-crystalline morphology exhibited fewer cracks after cycling (**Figures 6e** and **f**). This kind of structural robustness apparently results in less chemo-mechanical degradation compared to NMO, strongly contributing to its stability.

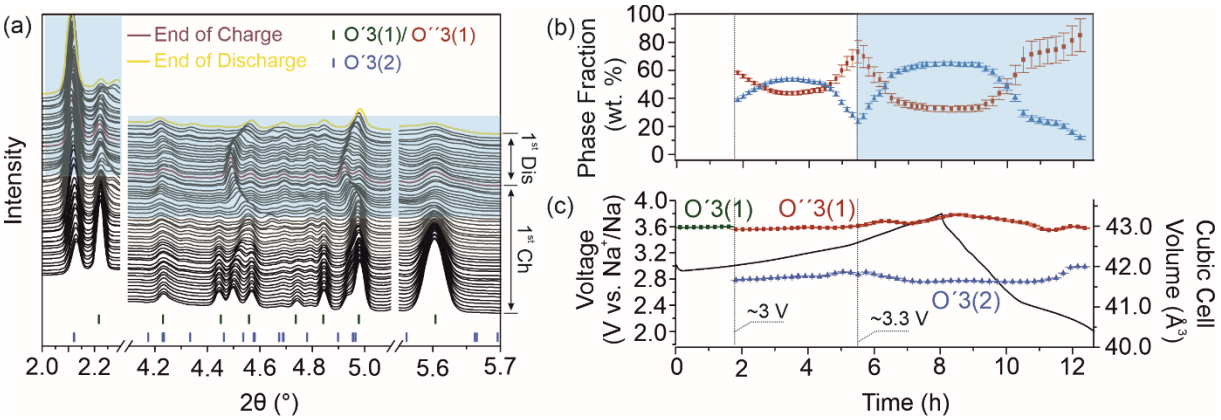

Figure 7. (a) *In situ* XRD patterns collected from the $NaMn_{0.9}Ti_{0.1}O_2$ (NMTO) cathode during cycling at C/10 shown in the form of a contour plot. (b) Phase fractions beyond 3.0 V vs. Na^+/Na and (c) corresponding volume variations.

To explore the structural changes occurring with NMTO during battery operation, *in situ* (synchrotron) XRD measurements were performed, as shown in **Figure 7a**. It is noteworthy that NMO (**Figure 1e**) exhibits eight distinct phases upon cycling, following the sequence O'3(1) → O'3(2) → O'3(3) → O'3(4) → O'3(5) → O'3(6) → O'3(7) → O'3-O1(8). As mentioned previously, among these, O'3(3) and O'3(5) correspond to triclinic phases, while the others are monoclinic. In contrast, for NMTO, only three monoclinic phases, namely O'3(1), the Na-deficient phase of O'3(1), and O'3(2), were detected,

with no P-type phase being present. This observation is consistent with Kobota *et al*.'s study on the structural evolution of NMO.[31] They argue that P-type phases are commonly observed in Ni-, Cr-, Co-, or Ni/Mn-based O3 and O'3-type $NaTMO_2$ cathodes during cycling but are typically introduced into Mn-based systems through solid-state synthesis.[43–46] Although Ma *et al*. reported on the presence of P-type phases in their study on NMO, the current results align with earlier findings.[47] For clarity, the Na-deficient phase of O'3(1) is hereafter referred to as O''3(1).

As shown in **Figure 7a**, the initial phase upon charging up to about 3.0 V vs. Na^+/Na was O'3(1). With further Na^+ extraction, a gradual transition occurred, leading to a biphasic region. Unlike most O3 or O'3 structures, which undergo complete transition after some biphasic region or solid-solution reaction, NMTO maintained the coexistence of both phases throughout the charging/discharging process. To provide a more intuitive comparison of phase fractions and volume variations, the corresponding curves are displayed in **Figures 7b** and **c**. Because O''3(1) is a Na-deficient derivative of O'3(1) with the same monoclinic structure, they share identical reflections in **Figure 7a**. The O'3(2) phase matches the reported $Na_{5/8}MnO_2$. Although O'3(2) also has a *C*2/*m* structure, the Bragg positions differ significantly.

In previous studies on NMO, it has been observed that structures similar to O'3(2) only exist within a state of charge (SOC) range of (5–40) %, after which further structural transformations occur.[28,31] For NMTO, based on the first-cycle specific charge capacity of $q_{ch} \approx 150$ mAh/g ($q_{th} = 245$ mAh/g), the SOC was about 61 %. However, NMTO did not undergo further transformations after transitioning toward O'3(2). A possible reason is that the introduction of Ti^{4+} effectively suppresses the Na-1/2 and Na-1/3 ordering, as well as the associated manganese valence ordering typically present in NMO. Instead, it seems to activate new sodium and/or manganese ordering, as also indicated by the additional features observed in the differential capacity curves shown in **Figure S3** (Supporting Information).[28] At the same time, the complete phase transition can be impeded, resulting in the coexistence of the O''3(1) and O'3(2) phases throughout cycling. From the XRD patterns in **Figure 7a**, it can be seen that NMTO did not revert back to the initial O'3(1) phase. The blue-shaded area highlights the reversible charge/discharge region, which was also maintained in the second charging process (**Figure S8**, Supporting Information) and followed a similar trend. These findings indicate that after the initial cycle, NMTO consistently alternates between O''3(1) and O'3(2), with the phase evolution following the trend illustrated in **Figure 7b**.

Taken together, the introduction of Ti^{4+} successfully prevents the formation of the O1 phase at high potentials. Consequently, the reduced volume changes (**Figure 7c**) lead to fewer particle fracture (**Figure 6f**), thus increasing cycling stability.

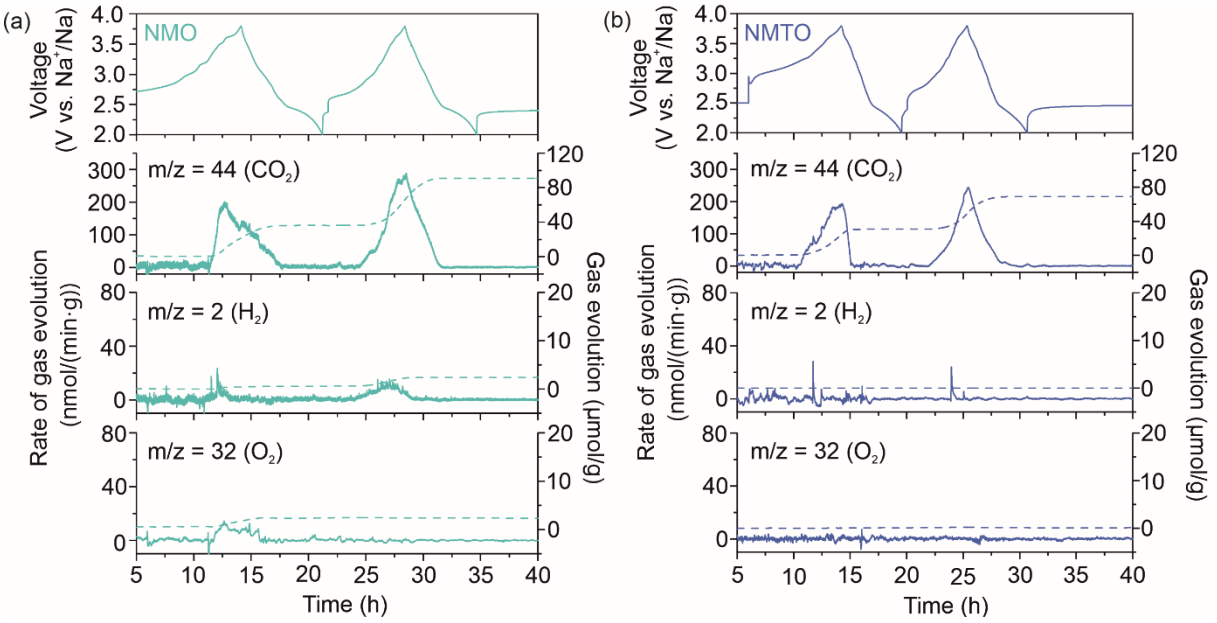

Figure 8. Voltage profiles of SIB half-cells using either (a) $NaMnO_2$ (NMO) or (b) $NaMn_{0.9}Ti_{0.1}O_2$ (NMTO) at C/10 and corresponding time-resolved evolution rates (left *y*-axis) and cumulative amounts (right *y*-axis) of CO_2, H_2, and O_2 measured by DEMS.

Despite extensive research on various aspects of NMO, including electrochemical properties and structural evolution, studies on its gassing behavior are lacking.[2,28,31] Here, to our knowledge, the first *in situ* gas analysis was conducted on NMO via DEMS. Furthermore, the same analysis was done with NMTO to unravel the effect of Ti^{4+} substitution on outgassing of NMO.

Both the NMO and NMTO cathodes were cycled at a rate of C/10 for two consecutive cycles in a customized battery configuration.[48,49] **Figures 8a** and **b** present the voltage profiles, gas evolution rates, and total amounts for the gases that evolved the most, namely oxygen (O_2, *m*/*z* = 32), hydrogen (H_2, *m*/*z* = 2), and carbon dioxide (CO_2, *m*/*z* = 44). Due to the limited studies available on gas evolution in SIBs and their similarities with LIBs, the gassing mechanism can be inferred from LIBs.[50,51] Generally, CO_2 originates from the electrochemical and/or chemical decomposition of surface carbonates,[52–54] the chemical oxidation of the electrolyte by lattice oxygen, or the electrochemical decomposition of the electrolyte at high potentials (> 4.7 V vs. Li^+/Li).[55] H_2 is typically generated from residual water or from protic species formed at high potentials at the cathode side, which subsequently migrate to the anode.[56] The formation of O_2 usually results from the loss of lattice oxygen. However, due to its high reactivity, O_2 often cannot be directly detected and instead is present in the form of CO_2.[57,58]

The gassing behavior of NMO and NMTO is illustrated in **Figures 8a** and **b**, respectively. NMO exhibited a significant release of CO_2 (36 µmol/g) in the initial cycle, along with some H_2 and O_2 evolution. Since CO_2 evolution already started at a relatively low potential, electrolyte oxidation as a reason for its generation can be largely ruled out. A small amount of O_2 (2.3 µmol/g) evolved in the same voltage

window, hinting at irreversible anion redox. Notably, gas evolution started at 3.25 V vs. Na^+/Na, coinciding with the phase transition of NMO to the O1 phase, where the generation of O_2 may be related to manganese migration.[28,31] The similar profiles observed for O_2 and CO_2 further corroborate that CO_2 is likely produced via chemical electrolyte oxidation by lattice oxygen. Aside from that, some of the CO_2 release in the initial cycle can also be attributed to the electrochemical oxidation of surface carbonates. Specifically, the Fourier-transform infrared spectroscopy (FTIR) data in **Figure S9** (Supporting Information) confirm the presence of residual carbonate species, while the ICP-OES results (**Table S3**, Supporting Information) indicate sodium excess. The minor release of H_2 is likely due to residual water being present in the sample or the cell parts or the formation of alcoholic species during cycling.

Unlike NMO, NMTO did not reveal noticeable H_2 or O_2 signals but still showed a significant amount of CO_2 evolution (31 µmol/g). Both **Figure S9** and **Table S3** (Supporting Information) indicate that NMTO contains a higher amount of residual carbonates than NMO, suggesting that a higher share of the CO_2 evolution likely originates from their decomposition, while the remaining CO_2 may result from electrolyte oxidation. Studies on LIBs have shown that the oxidation of lithium carbonates on the $LiNi_xCo_yMn_zO_2$ (NCM) surface can also trigger the release of lattice oxygen, implying a similar mechanism may be at play here.[59] Additionally, the contribution of electrochemical electrolyte oxidation at high potentials cannot be entirely ruled out. Therefore, all of the aforementioned factors may contribute to the observed CO_2 evolution in the initial cycle.

In the second cycle, the peak CO_2 release rates increased, reaching 286 and 243 nmol/min/g for NMO and NMTO, respectively. This may be related to electrode breathing. Polycrystalline NMO likely exposes more reactive (fresh) surfaces than the quasi single-crystal NMTO particles in the initial cycle, meaning previously encapsulated/isolated species are becoming prone to adverse side reactions (oxidation). A similar trend has been observed in studies on poly- and single-crystalline $LiNi_{0.6}Co_{0.2}Mn_{0.2}O_2$ cathodes in LIBs.[60] Notably, previous DFT studies on $Na_{2/3}Mg_{1/3}Ti_{1/6}Mn_{1/2}O_2$ have shown that in the Ti^{4+}–O bonding case (d^0 configuration), electrons are more localized around the oxygen compared to Mn^{4+}–O bonding, which may positively affect the reversibility of anion redox.[61] Consequently, Ti^{4+} in NMTO may play a similar role in mitigating irreversible lattice oxygen loss (chemical electrolyte oxidation), ultimately leading to lower CO_2 evolution.

Conclusions

In summary, Ti^{4+} as a structural stabilizer was successfully introduced into NMO. Electrochemical testing identified 10 mol.% as the optimal degree of substitution. Laboratory and synchrotron XRD revealed that titanium incorporation not only increases the interslab distance but also prevents the unfavorable transition to the O1 phase at high potentials. Additionally, it facilitates the transition from polycrystalline to single-crystal material.

Overall, NMTO outperformed NMO in terms of cycling perfromance and stability. Specifically, its quasi single-crystalline morphology mitigates particle fracture, while the presence of titanium helps suppress irreversible oxygen redox during battery operation.

Experimental Section

Synthesis. $NaMn_{1-x}Ti_xO_2$ ($0 \leq x \leq 0.3$) cathode materials were synthesized via a single-step solid-state reaction. To this end, Mn_3O_4 ($d_{50} \approx 14$ µm, BASF Shanshan Battery Materials Co. Ltd.), nanosized TiO_2, and Na_2CO_3 (99.9%, Sigma-Aldrich) were accurately weighed in molar ratios of $(1-x):x:1.05$ and then homogenized for 10 min under an argon atmosphere using a high-speed laboratory blender (Kinematica) to ensure uniform mixing. The resulting precursor mixture was transferred to an alumina crucible and calcined at 800 °C for 12 h in a tube furnace (Nabertherm RHTC80/230/16) under a constant flow (7 L/h) of air. The heating rate was maintained at 5 K/min. Upon completion of the calcination cycle, the sample was quenched to ambient temperature.

Battery Testing. Electrode fabrication was carried out by casting a slurry consisting of 80 wt.% cathode material, 10 wt.% Super C65 conductive carbon, and 10 wt.% polyvinylidene difluoride (PVDF, Solef 5130, Solvay) binder dispersed in N-methyl-2-pyrrolidone (NMP). The slurry was homogenized using a planetary centrifugal mixer (Thinky ARE-250) at sequential speeds of 2000 and 400 rpm for a total of 6 min. Subsequently, it was deposited onto aluminum foil (30 µm thickness), serving as the current collector, using a film applicator (Erichsen Coatmaster 510) at a coating speed of 5 mm/s. The cathode sheet was dried under a dynamic vacuum at 120 °C, followed by calendaring at a line pressure of 14 N/mm (Sumet Messtechnik) to increase density. Circular electrodes with a diameter of 13 mm and areal mass loading of (6 ± 1) mg/cm^2 were punched and used for cell assembly.

CR2032-type coin cells were assembled in an argon glovebox using sodium metal as the counter/reference electrode, GF/D glass fiber as the separator, as well as 95 µL of electrolyte. The electrolyte consisted of 1 M $NaClO_4$ in a mixture of ethylene carbonate (EC), dimethyl carbonate (DMC), and propylene carbonate (PC) in a volumetric ratio of 1:1:1, with 5 vol.% fluoroethylene carbonate (FEC) additive. A battery cycler from MACCOR Inc. was used for electrochemical testing via galvanostatic cycling in a voltage window of 2.0–3.8 V vs. Na^+/Na, with a constant voltage step at 3.8 V maintained either for 30 min or until the current decreased below C/100 and with 1C being defined as 200 mA/g.

Laboratory X-ray Diffraction. Powder XRD measurements were performed in Debye-Scherrer geometry using a STOE STADI-P diffractometer (STOE & Cie GmbH) equipped with a molybdenum anode ($\lambda = 0.70926$ Å, 50 kV, 40 mA) and a DECTRIS MYTHEN 1K strip detector. For data acquisition, the samples were sealed in 0.5 mm diameter borosilicate glass capillaries (Hilgenberg) of wall thickness 0.01 mm. For line profile analysis, the instrumental broadening was assessed by collecting diffraction data from a LaB_6 standard reference material (NIST SRM 660c).

***In Situ* Synchrotron X-ray Diffraction.** Synchrotron XRD measurements were performed at the Powder Diffraction and Total Scattering beamline P02.1 of PETRA III, DESY (Hamburg, Germany)[62] using customized electrochemical cells (with Kapton windows) mounted in a dedicated sample holder, as described by Herklotz *et al.*[63] The wavelength of the incident beam was calibrated to $\lambda = 0.20726$ Å through refinement of diffraction data collected from a LaB_6 standard reference material (NIST SRM 660c). Electrochemical cycling commenced only after acquisition of the initial diffraction pattern to accurately capture the pristine state of the cathode materials. To prevent interference from aluminum signals, the samples were cast onto carbon tape. Note that the inherent porosity of the latter may lead to non-uniform coating. The cells were cycled galvanostatically at a rate of C/10, and diffraction patterns were recorded using a VAREX 4343CT area detector (150 × 150 μm^2 pixel size, 2880 × 2880 pixel area, CsI scintillator directly deposited on amorphous Si photodiodes) with an exposure time of 130 s per scan. Detector calibration was accomplished using the NIST SRM 660c sealed in a coin cell. 2D images were integrated using the pyFAI software package,[64] and subsequent structural analysis was performed via Rietveld refinement employing the FullProf Suite software.

Scanning Electron Microscopy. SEM images were acquired on a LEO-1530 field emission microscope (Carl Zeiss AG) at an accelerating voltage of 10 kV. For cross-sectional analysis, specimens were prepared using an ion beam cross-section polisher (JEOL IB-19510CP) equipped with an argon ion source.

Transmission Electron Microscopy. TEM measurements were performed on an image-corrected Titan Themis (Thermo Fisher Scientific) at an accelerating voltage of 300 kV. Chemical composition mapping was carried out using a SuperX EDS detector in scanning TEM mode. Cross-sectional specimens were prepared by FIB milling using a SARATA (FEI) dual beam with a gallium ion source. The samples were exposed to ambient conditions for about 5 min during FIB preparation. The FIB lamella was milled at 30 kV initially, followed by final polishing with 2 kV to minimize surface damage. Cathode material was dispersed onto holey C-Cu grids inside an argon glovebox and then transferred for investigation.

Inductively Coupled Plasma-Optical Emission Spectroscopy. The elemental composition of samples was determined by ICP-OES using an ICAP 7600 DUO instrument (Thermo Fisher Scientific). About 10 mg of cathode material was digested in a graphite furnace using a mixture of hydrochloric acid and nitric acid at 353 K for 4 h. The resulting solutions were diluted and analyzed against four external calibration standards, with scandium serving as an internal standard. For each sample, measurements were repeated three times. The oxygen content was determined by carrier gas hot extraction using a TC600 oxygen/nitrogen analyzer (LECO Corp.), with calibration performed against the certified reference material KED-1025.

High-energy-resolution Fluorescence Detected X-ray Absorption Near-edge Structure Spectroscopy. HERFD-XANES spectroscopy was performed at beamline ID26 of the European Synchrotron Radiation Facility (Grenoble, France), a high-brilliance undulator beamline optimized for advanced X-ray spectroscopic studies.

Both pristine and cycled cathodes (20 cycles at C/10) were sealed using Kapton tape to minimize air exposure and measured under ambient conditions. To mitigate potential beam-induced damage, multiple spectra were recorded for each sample. Energy calibration was done by aligning the first inflection point in the first derivative of μ(E) from a titanium reference foil. Spectral normalization and averaging (over 15 individual scans) were performed using the PyMca software package (version 5.9.2).[65]

Differential Electrochemical Mass Spectrometry. DEMS measurements were conducted on customized half-cells with cathodes of 30 mm diameter and an areal mass loading of about 10 mg/cm^2 using 700 µL of the aforementioned electrolyte. Electrochemical cycling was performed at a rate of C/10. A continuous flow of helium (purity grade 6.0, 2.5 mL/min) as the carrier gas was maintained through the cell. The evolved gases were extracted in real-time and analyzed using a mass spectrometer (OmniStar GSD 320, Pfeiffer Vacuum GmbH).[48,49]

Fourier-transform Infrared Spectroscopy. FTIR spectroscopy was performed under an inert atmosphere within an argon glovebox (to prevent sample degradation upon exposure to air/moisture) using an ALPHA FT-IR spectrometer (Bruker) equipped with a germanium crystal.

Associated Content

Supporting Information

SEM image and XRD pattern of the Mn_3O_4 precursor cathode material, additional electrochemical data, XANES spectra, STEM-EDS mapping, *in situ* XRD patterns, FTIR spectra, and tables summarizing structural parameters and phase fractions from Rietveld analyses, as well as ICP-OES results.

Notes

The authors declare no competing financial interest.

Acknowledgments

This study was supported by BASF SE. The authors thank Dr. Thomas Bergfeldt (KIT), Dr. Yang Hu (HIU), and Dr. Jing Lin (KIT) for helping collect the ICP-OES and XANES data, respectively. We acknowledge the ESRF for provision of synchrotron radiation facilities under proposal no. MA-6219 (DOI: 10.15151/ESRF-ES-1550923205). We also thank Dr. Sami Juhani Vasala for assistance and support in using beamlines ID26. We acknowledge DESY, a member of the Helmholtz Association (HGF), for the provision of experimental facilities. Parts of this research were carried out at PETRA III, and we thank Dr. Volodymyr Baran for assistance in using beamline P02.1. Beamtime was allocated for proposal I-20230867. The lead authors are grateful to the Federal Ministry of Education and Research (BMBF) for funding within the project ENTISE (03XP0579K).

References

(1) Yabuuchi, N.; Kubota, K.; Dahbi, M.; Komaba, S. Research Development on Sodium-Ion Batteries, *Chem. Rev.* **2014**, *114*, 11636–11682. https://doi.org/10.1021/cr500192f.

(2) Ma, X.; Chen, H.; Ceder, G. Electrochemical Properties of Monoclinic $NaMnO_2$, *J. Electrochem. Soc.* **2011**, *158*, A1307–A1312. https://doi.org/10.1149/2.035112jes.

(3) Manthiram, A. A reflection on lithium-ion battery cathode chemistry, *Nat. Commun.* **2020**, *11*, 1550. https://doi.org/10.1038/s41467-020-15355-0.

(4) Chang, U.; Lee, J. T.; Yun, J.-M.; Lee, B.; Lee, S. W.; Joh, H.-I.; Eom, K.; Fuller, T. F. *In Situ* Self-Formed Nanosheet MoS_3/Reduced Graphene Oxide Material Showing Superior Performance as a Lithium-Ion Battery Cathode, *ACS Nano* **2019**, *13*, 1490–1498. https://doi.org/10.1021/acsnano.8b07191.

(5) Yuan, T.; Li, S.; Sun, Y.; Wang, J.-H.; Chen, A.-J.; Zheng, Q.; Zhang, Y.; Chen, L.; Nam, G.; Che, H.; Yang, J.; Zheng, S.; Ma, Z.-F.; Liu, M. A High-Rate, Durable Cathode for Sodium-Ion Batteries: Sb-Doped O3-Type Ni/Mn-Based Layered Oxides, *ACS Nano* **2022**, *16*, 18058–18070. https://doi.org/10.1021/acsnano.2c04702.

(6) Chayambuka, K.; Mulder, G.; Danilov, D. L.; Notten, P. H. L. Sodium-Ion Battery Materials and Electrochemical Properties Reviewed, *Adv. Energy Mater.* **2018**, *8*, 1800079. https://doi.org/10.1002/aenm.201800079.

(7) Li, S.; Sun, Y.; Pang, Y.; Xia, S.; Chen, T.; Sun, H.; Zheng, S.; Yuan, T. Recent developments of layered transition metal oxide cathodes for sodium-ion batteries toward desired high performance, *Asia-Pac. J. Chem. Eng.* **2022**, *17*, e2762. https://doi.org/10.1002/apj.2762.

(8) Gao, R.-M.; Zheng, Z.-J.; Wang, P.-F.; Wang, C.-Y.; Ye, H.; Cao, F.-F. Recent advances and prospects of layered transition metal oxide cathodes for sodium-ion batteries, *Energy Storage Mater.* **2020**, *30*, 9–26. https://doi.org/10.1016/j.ensm.2020.04.040.

(9) You, Y.; Xin, S.; Asl, H. Y.; Li, W.; Wang, P.-F.; Guo, Y.-G.; Manthiram, A. Insights into the Improved High-Voltage Performance of Li-Incorporated Layered Oxide Cathodes for Sodium-Ion Batteries, *Chem* **2018**, *4*, 2124–2139. https://doi.org/10.1016/j.chempr.2018.05.018.

(10) Kubota, K.; Dahbi, M.; Hosaka, T.; Kumakura, S.; Komaba, S. Towards K-Ion and Na-Ion Batteries as “Beyond Li-Ion,” *Chem. Rec.* **2018**, *18*, 459–479. https://doi.org/10.1002/tcr.201700057.

(11) Massé, R. C.; Uchaker, E.; Cao, G. Beyond Li-ion: electrode materials for sodium- and magnesium-ion batteries, *Sci. China Mater.* **2015**, *58*, 715–766. https://doi.org/10.1007/s40843-015-0084-8.

(12) Elia, G. A.; Kravchyk, K. V.; Kovalenko, M. V.; Chacón, J.; Holland, A.; Wills, R. G. A. An overview and prospective on Al and Al-ion battery technologies, *J. Power Sources* **2021**, *481*, 228870. https://doi.org/10.1016/j.jpowsour.2020.228870.

(13) Han, M. H.; Gonzalo, E.; Singh, G.; Rojo, T. A comprehensive review of sodium layered oxides: powerful cathodes for Na-ion batteries, *Energy Environ. Sci.* **2015,** *8*, 81–102. https://doi.org/10.1039/c4ee03192j.

(14) Wang, P.-F.; You, Y.; Yin, Y.-X.; Wang, Y.-S.; Wan, L.-J.; Gu, L.; Guo, Y.-G. Suppressing the P2–O2 Phase Transition of $Na_{0.67}Mn_{0.67}Ni_{0.33}O_2$ by Magnesium Substitution for Improved Sodium-Ion Batteries, *Angew. Chem. Int. Ed.* **2016**, *128*, 7571–7575. https://doi.org/10.1002/ange.201602202.

(15) Guo, S.; Yu, H.; Liu, P.; Ren, Y.; Zhang, T.; Chen, M.; Ishida, M.; Zhou, H. High-performance symmetric sodium-ion batteries using a new, bipolar O3-type material, $Na_{0.8}Ni_{0.4}Ti_{0.6}O_2$, *Energy Environ. Sci.* **2015**, *8*, 1237–1244. https://doi.org/10.1039/c4ee03361b.

(16) Wang, P.-F.; Yao, H.-R.; Liu, X.-Y.; Zhang, J.-N.; Gu, L.; Yu, X.-Q.; Yin, Y.-X.; Guo, Y.-G. Ti-Substituted $NaNi_{0.5}Mn_{0.5-x}Ti_xO_2$ Cathodes with Reversible O3−P3 Phase Transition for High-Performance Sodium-Ion Batteries, *Adv. Mater.* **2017**, *29*, 1700210. https://doi.org/10.1002/adma.201700210.

(17) Delmas, C.; Fouassier, C.; Hagenmuller, P. Structural classification and properties of the layered oxides, *Physica B+C* **1980**, *99,* 81–85. https://doi.org/10.1016/0378-4363(80)90214-4.

(18) Xie, Y.; Gabriel, E.; Fan, L.; Hwang, I.; Li, X.; Zhu, H.; Ren, Y.; Sun, C.; Pipkin, J.; Dustin, M.; Li, M.; Chen, Z.; Lee, E.; Xiong, H. Role of Lithium Doping in P2-$Na_{0.67}Ni_{0.33}Mn_{0.67}O_2$ for Sodium-Ion Batteries, *Chem. Mater.* **2021**, *33*, 4445–4455. https://doi.org/10.1021/acs.chemmater.1c00569.

(19) Delmas, C.; Braconnier, J.-J.; Fouassier, C.; Hagenmuller, P. Electrochemical intercalation of sodium in Na_xCoO_2 bronzes, *Solid State Ion.* **1981**, *3–4*, 165–169. https://doi.org/10.1016/0167-2738(81)90076-X.

(20) Guo, S.; Liu, P.; Yu, H.; Zhu, Y.; Chen, M.; Ishida, M.; Zhou, H. A Layered P2- and O3-Type Composite as a High-Energy Cathode for Rechargeable Sodium-Ion Batteries, *Angew. Chem. Int. Ed.* **2015**, *54*, 5894–5899. https://doi.org/10.1002/anie.201411788.

(21) Wang, J.; Dreyer, S. L.; Wang, K.; Ding, Z.; Diemant, T.; Karkera, G.; Ma, Y.; Sarkar, A.; Zhou, B.; Gorbunov, M. V.; Omar, A.; Mikhailova, D.; Presser, V.; Fichtner, M.; Hahn, H.; Brezesinski, T.; Breitung, B.; Wang, Q. P2-type layered high-entropy oxides as sodium-ion cathode materials. *Mater. Futures* **2022**, *1*, 035104. https://doi.org/10.1088/2752-5724/ac8ab9.

(22) Wei, F.; Zhang, Q.; Zhang, P.; Tian, W.; Dai, K.; Zhang, L.; Mao, J.; Shao, G. Review—Research Progress on Layered Transition Metal Oxide Cathode Materials for Sodium Ion Batteries, *J. Electrochem. Soc.* **2021**, *168*, 050524. https://doi.org/10.1149/1945-7111/abf9bf.

(23) Guo, Z.; Li, X.; Lyu, Y.; Xu, S. Improved electrochemical performance of B doped O'3-$NaMnO_2$ for Na-ion battery, *Electrochim. Acta* **2022**, *430*, 141079. https://doi.org/10.1016/j.electacta.2022.141079.

(24) Kumakura, S.; Tahara, Y.; Kubota, K.; Chihara, K.; Komaba, S. Sodium and Manganese Stoichiometry of P2-Type $Na_{2/3}MnO_2$, *Angew. Chem. Int. Ed.* **2016**, *55*, 12760–12763. https://doi.org/10.1002/anie.201606415.

(25) Yabuuchi, N.; Kajiyama, M.; Iwatate, J.; Nishikawa, H.; Hitomi, S.; Okuyama, R.; Usui, R.; Yamada, Y.; Komaba, S. P2-type $Na_x[Fe_{1/2}Mn_{1/2}]O_2$ made from earth-

abundant elements for rechargeable Na batteries, *Nat. Mater.* **2012**, *11*, 512–517. https://doi.org/10.1038/nmat3309.

(26) Sathiya, M.; Thomas, J.; Batuk, D.; Pimenta, V.; Gopalan, R.; Tarascon, J.-M. Dual Stabilization and Sacrificial Effect of Na_2CO_3 for Increasing Capacities of Na-Ion Cells Based on P2-Na_xMO_2 Electrodes, *Chem. Mater.* **2017**, *29*, 5948–5956. https://doi.org/10.1021/acs.chemmater.7b01542.

(27) Matsuzaki, M.; Tatara, R.; Kubota, K.; Kuroki, K.; Hosaka, T.; Umetsu, K.; Okada, N.; Komaba, S. Application of Na_2CO_3 as a Sacrificial Electrode Additive in Na-ion Batteries to Compensate for the Sodium Deficiency in $Na_{2/3}[Fe_{1/2}Mn_{1/2}]O_2$, *Batter. Supercaps* **2024**, *7*, e202400009. https://doi.org/10.1002/batt.202400009.

(28) Chen, X.; Wang, Y.; Wiaderek, K.; Sang, X.; Borkiewicz, O.; Chapman, K.; LeBeau, J.; Lynn, J.; Li, X. Super Charge Separation and High Voltage Phase in Na_xMnO_2, *Adv. Funct. Mater.* **2018**, *28*, 1805105. https://doi.org/10.1002/adfm.201805105.

(29) Manzi, J.; Paolone, A.; Palumbo, O.; Corona, D.; Massaro, A.; Cavaliere, R.; Muñoz-García, A. B.; Trequattrini, F.; Pavone, M.; Brutti, S. Monoclinic and Orthorhombic $NaMnO_2$ for Secondary Batteries: A Comparative Study, *Energies* **2021**, *14*, 1230. https://doi.org/10.3390/en14051230.

(30) Shishkin, M.; Kumakura, S.; Sato, S.; Kubota, K.; Komaba, S.; Sato, H. Unraveling the Role of Doping in Selective Stabilization of $NaMnO_2$ Polymorphs: Combined Theoretical and Experimental Study, *Chem. Mater.* **2018**, *30*, 1257–1264. https://doi.org/10.1021/acs.chemmater.7b04394.

(31) Kubota, K.; Miyazaki, M.; Kim, E. J.; Yoshida, H.; Barpanda, P.; Komaba, S. Structural change induced by electrochemical sodium extraction from layered O′3-$NaMnO_2$, *J. Mater. Chem. A* **2021**, *9*, 26810–26819. https://doi.org/10.1039/d1ta05390f.

(32) Yu, H.; Guo, S.; Zhu, Y.; Ishida, M.; Zhou, H. Novel titanium-based O3-type $NaTi_{0.5}Ni_{0.5}O_2$ as a cathode material for sodium ion batteries, *Chem. Commun.* **2014**, *50*, 457–459. https://doi.org/10.1039/C3CC47351A.

(33) Maletti, S.; Sarapulova, A.; Schökel, A.; Mikhailova, D. Operando Studies on the $NaNi_{0.5}Ti_{0.5}O_2$ Cathode for Na-Ion Batteries: Elucidating Titanium as a Structure Stabilizer, *ACS Appl. Mater. Interfaces* **2019**, *11*, 33923–33930. https://doi.org/10.1021/acsami.9b10352.

(34) An, S.; Karger, L.; Dreyer, S. L.; Hu, Y.; Barbosa, E.; Zhang, R.; Lin, J.; Fichtner, M.; Kondrakov, A.; Janek, J.; Brezesinski, T. Improving cycling performance of the $NaNiO_2$ cathode in sodium-ion batteries by titanium substitution, *Mater. Futures* **2024**, *3*, 035103. https://doi.org/10.1088/2752-5724/ad5faa.

(35) Sato, T.; Yoshikawa, K.; Zhao, W.; Kobayashi, T.; Rajendra, H. B.; Yonemura, M.; Yabuuchi, N. Efficient Stabilization of Na Storage Reversibility by Ti Integration into O′3-Type $NaMnO_2$, *Energy Mater. Adv.* **2021**, *2021*, 9857563. https://doi.org/10.34133/2021/9857563.

(36) Vassilaras, P.; Ma, X.; Li, X.; Ceder, G. Electrochemical Properties of Monoclinic $NaNiO_2$, *J. Electrochem. Soc.* **2013**, *160*, A207–A211. https://doi.org/10.1149/2.023302jes.

(37) Jo, I.-H.; Ryu, H.-S.; Gu, D.-G.; Park, J.-S.; Ahn, I.-S.; Ahn, H.-J.; Nam, T.-H.; Kim, K.-W. The effect of electrolyte on the electrochemical properties of Na/*α*-

$NaMnO_2$ batteries, *Mater. Res. Bull.* **2014**, *58*, 74–77. https://doi.org/10.1016/j.materresbull.2014.02.024.

(38) An, S.; Karger, L.; Müller, P.; Lin, J.; Vasala, S.; Baran, V.; Dreyer, S. L.; Zhang, R.; Ulusoy, F.; Kondrakov, A.; Janek, J.; Brezesinski, T. Exploring calcium pillaring of O3-type $NaNi_{0.9}Ti_{0.1}O_2$ cathodes to advance Na-ion battery technology. *Chem. Eng. J.* **2025**, *509*, 160939. https://doi.org/10.1016/j.cej.2025.160939.

(39) Ryu, H.-H.; Park, K.-J.; Yoon, D. R.; Aishova, A.; Yoon, C. S.; Sun,Y.-K. $Li[Ni_{0.9}Co_{0.09}W_{0.01}]O_2$: A New Type of Layered Oxide Cathode with High Cycling Stability, *Adv. Energy Mater.* **2019**, *9*, 1902698. https://doi.org/10.1002/aenm.201902698.

(40) Ma, Q.; Li, R.; Zheng, R.; Liu, Y.; Huo, H.; Dai, C. Improving rate capability and decelerating voltage decay of Li-rich layered oxide cathodes via selenium doping to stabilize oxygen, *J. Power Sources* **2016**, *331*, 112–121. https://doi.org/10.1016/j.jpowsour.2016.08.137.

(41) Wang, C.-C.; Manthiram, A. Influence of cationic substitutions on the first charge and reversible capacities of lithium-rich layered oxide cathodes, *J. Mater. Chem. A* **2013**, *1*, 10209–10217. https://doi.org/10.1039/c3ta11703k.

(42) Guo, S.; Yu, H.; Liu, D.; Tian, W.; Liu, X.; Hanada, N.; Ishid, M.; Zhou, H. A novel tunnel $Na_{0.61}Ti_{0.48}Mn_{0.52}O_2$ cathode material for sodium-ion batteries, *Chem. Commun.* **2014**, *50*, 7998–8001. https://doi.org/10.1039/c4cc02362e.

(43) Yu, T.-Y.; Ryu, H.-H.; Han, G.; Sun, Y.-K, Understanding the Capacity Fading Mechanisms of O3-Type $Na[Ni_{0.5}Mn_{0.5}]O_2$ Cathode for Sodium-Ion Batteries, *Adv. Energy Mater.* **2020**, *10*, 2001609. https://doi.org/10.1002/aenm.202001609.

(44) Braconnier, J.-J.; Delmas, C.; Fouassier, C.; Hagenmuller, P. Comportement electrochimique des phases Na_xCoO_2, *Mater. Res. Bull.* **1980**, *15*, 1797–1804. https://doi.org/10.1016/0025-5408(80)90199-3.

(45) Kubota, K.; Ikeuchi, I.; Nakayama, T.; Takei, C.; Yabuuchi, N.; Shiiba, H.; Nakayama, M.; Komaba, S. New Insight into Structural Evolution in Layered $NaCrO_2$ during Electrochemical Sodium Extraction, *J. Phys. Chem. C* **2015**, *119*, 166–175. https://doi.org/10.1021/jp5105888.

(46) Huang, Q.; Liu, J.; Zhang, L.; Xu, S.; Chen, L.; Wang, P.; Ivey, D. G.; Wei, W. Tailoring alternating heteroepitaxial nanostructures in Na-ion layered oxide cathodes via an *in-situ* composition modulation route, *Nano Energy* **2018**, *44*, 336–344. https://doi.org/10.1016/j.nanoen.2017.12.014.

(47) Ma, T.; Xu, G.-L.; Li, Y.; Song, B.; Zeng, X.; Su, C.-C.; Mattis, W. L.; Guo, F.; Ren, Y.; Kou, R.; Sun, C.; Heald, S. M.; Wang, H.-H.; Shahbazian-Yassar, R.; Jorne, J.; Chen, Z.; Amine, K. Insights into the Performance Degradation of Oxygen-Type Manganese-Rich Layered Oxide Cathodes for High-Voltage Sodium-Ion Batteries, *ACS Appl. Energy Mater.* **2018**, *1*, 5735–5745. https://doi.org/10.1021/acsaem.8b01325.

(48) Berkes, B. B.; Jozwiuk, A.; Vračar, M.; Sommer, H.; Brezesinski, T.; Janek, J. Online Continuous Flow Differential Electrochemical Mass Spectrometry with a Realistic Battery Setup for High-Precision, Long-Term Cycling Tests, *Anal. Chem.* **2015**, *87*, 5878–5883. https://doi.org/10.1021/acs.analchem.5b01237.

(49) Berkes, B. B.; Jozwiuk, A.; Sommer, H.; Brezesinski, T.; Janek, J. Simultaneous acquisition of differential electrochemical mass spectrometry and infrared spectroscopy data for in situ characterization of gas evolution reactions in lithium-ion batteries, *Electrochem. Commun.* **2015**, *60*, 64–69. https://doi.org/10.1016/j.elecom.2015.08.002.

(50) Zhang, L.; Tsolakidou, C.; Mariyappan, S.; Tarascon, J.-M.; Trabesinger, S. Unraveling gas evolution in sodium batteries by online electrochemical mass spectrometry, *Energy Storage Mater.* **2021**, *42*, 12–21. https://doi.org/10.1016/j.ensm.2021.07.005.

(51) Dreyer, S. L.; Kondrakov, A.; Janek, J.; Brezesinski, T. In situ analysis of gas evolution in liquid- and solid-electrolyte-based batteries with current and next-generation cathode materials. *J. Mater. Res.* **2022**, *37*, 3146–3168. https://doi.org/10.1557/s43578-022-00586-2.

(52) Mahne, N.; Renfrew, S. E.; McCloskey, B. D.; Freunberger, S. A. Electrochemical Oxidation of Lithium Carbonate Generates Singlet Oxygen, *Angew. Chem. Int. Ed.* **2018**, *57*, 5529–5533. https://doi.org/10.1002/anie.201802277.

(53) Freiberg, A. T. S.; Sicklinger, J.; Solchenbach, S.; Gasteiger, H. A. Li_2CO_3 decomposition in Li-ion batteries induced by the electrochemical oxidation of the electrolyte and of electrolyte impurities, *Electrochim. Acta* **2020**, *346*, 136271. https://doi.org/10.1016/j.electacta.2020.136271.

(54) Strauss, F.; Payandeh, S.; Kondrakov, A.; Brezesinski, T. On the role of surface carbonate species in determining the cycling performance of all-solid-state batteries. *Mater. Futures* **2022**, *1*, 023501. https://doi.org/10.1088/2752-5724/ac5b7d.

(55) Jung, R.; Metzger, M.; Maglia, F.; Stinner, C.; Gasteiger, H. A. Chemical versus Electrochemical Electrolyte Oxidation on NMC111, NMC622, NMC811, LNMO, and Conductive Carbon, *J. Phys. Chem. Lett.* **2017**, *8*, 4820–4825. https://doi.org/10.1021/acs.jpclett.7b01927.

(56) Metzger, M.; Strehle, B.; Solchenbach, S.; Gasteiger, H. A. Origin of H_2 Evolution in LIBs: H_2O Reduction vs. Electrolyte Oxidation, *J. Electrochem. Soc.* **2016**, *163*, A798–A809. https://doi.org/10.1149/2.1151605jes.

(57) Jung, R.; Metzger, M.; Maglia, F.; Stinner, C.; Gasteiger, H. A. Oxygen Release and Its Effect on the Cycling Stability of $LiNi_xMn_yCo_zO_2$ (NMC) Cathode Materials for Li-Ion Batteries, *J. Electrochem. Soc.* **2017**, *164*, A1361–A1377. https://doi.org/10.1149/2.0021707jes.

(58) Wandt, J.; Freiberg, A. T. S.; Ogrodnik, A.; Gasteiger, H. A. Singlet oxygen evolution from layered transition metal oxide cathode materials and its implications for lithium-ion batteries, *Mater. Today* **2018**, *21*, 825–833. https://doi.org/10.1016/j.mattod.2018.03.037.

(59) Kaufman, L. A.; McCloskey, B. D. Surface Lithium Carbonate Influences Electrolyte Degradation via Reactive Oxygen Attack in Lithium-Excess Cathode Materials, *Chem. Mater.* **2021**, *33*, 4170–4176. https://doi.org/10.1021/acs.chemmater.1c00935.

(60) Oswald, S.; Bock, M.; Gasteiger, H. A. Elucidating the Implications of Morphology on Fundamental Characteristics of Nickel-Rich NCMs: Cracking,

Gassing, Rate Capability, and Thermal Stability of Poly- and Single-Crystalline NCM622, *J. Electrochem. Soc.* **2022**, *169*, 050501. https://doi.org/10.1149/1945-7111/ac5f7f.

(61) Zhao, C.; Yao, Z.; Wang, J.; Lu, Y.; Bai, X.; Aspuru-Guzik, A.; Chen, L.; Hu, Y.-S. Ti Substitution Facilitating Oxygen Oxidation in $Na_{2/3}Mg_{1/3}Ti_{1/6}Mn_{1/2}O_2$ Cathode, *Chem* **2019**, *5*, 2913–2925. https://doi.org/10.1016/j.chempr.2019.08.003.

(62) Dippel, A.-C.; Liermann, H.-P.; Delitz, J. T.; Walter, P.; Schulte-Schrepping, H.; Seeck, O. H.; Franz, H. Beamline P02.1 at PETRA III for high-resolution and high-energy powder diffraction, *J. Synchrotron Rad.* **2015**, *22*, 675–687. https://doi.org/10.1107/S1600577515002222.

(63) Herklotz, M.; Weiß, J.; Ahrens, E.; Yavuz, M.; Mereacre, L.; Kiziltas-Yavuz, N.; Dräger, C.; Ehrenberg, H.; Eckert, J.; Fauth, F.; Giebeler, L.; Knapp, M. A novel high-throughput setup for in situ powder diffraction on coin cell batteries, *J. Appl. Cryst.* **2016**, *49*, 340–345. https://doi.org/10.1107/S1600576715022165.

(64) Ashiotis, G.; Deschildre, A.; Nawaz, Z.; Wright, J. P.; Karkoulis, D.; Picca, F. E.; Kieffer, J. The fast azimuthal integration Python library: pyFAI, *J. Appl. Cryst.* **2015**, *48*, 510–519. https://doi.org/10.1107/S1600576715004306.

(65) Solé, V. A.; Papillon, E.; Cotte, M.; Walter, Ph.; Susini, J. A multiplatform code for the analysis of energy-dispersive X-ray fluorescence spectra, *Spectrochim. Acta Part B* **2007**, *62*, 63–68. https://doi.org/10.1016/j.sab.2006.12.002.

TOC

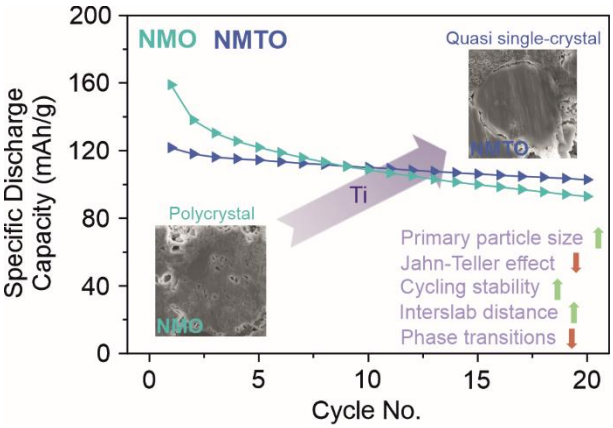
NMO
NMTO
Quasi single-crystal
Polycrystal
Ti
Primary particle size
Jahn-Teller effect
Cycling stability
Interslab distance
Phase transitions
Specific Discharge Capacity (mAh/g)
Cycle No.
200
160
120
80
40
0
0
5
10
15
20